

Synthesis of Rhenium-Doped Molybdenum Sulfide by Atmospheric Pressure Chemical Vapor Deposition (CVD) for a High-Performance Photodetector

Xinke Liu, Jiangchuan Wang, Yuheng Lin, Jie Zhou, Qiang Liu, Wenjie Yu, Yongqing Cai, Xiaohua Li, V. Divakar Botcha, Tingke Rao, and Shuangwu Huang*



Cite This: *ACS Omega* 2022, 7, 48301–48309



Read Online

ACCESS |



Metrics & More



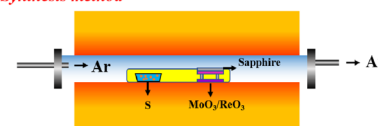
Article Recommendations



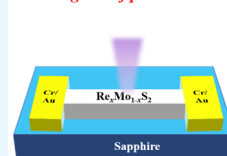
Supporting Information

ABSTRACT: Two-dimensional layered materials have attracted tremendous attention as photodetectors due to their fascinating features, including comprehensive coverage of band gaps, high potential in new-generation electronic devices, mechanical flexibility, and sensitive light–mass interaction. Currently, graphene and transition-metal dichalcogenides (TMDCs) are the most attractive active materials for constructing photodetectors. A growing number of emerging TMDCs applied in photodetectors bring up opportunities in the direct band gap independence with thickness. This study demonstrated for the first time a photodetector based on a few-layer $\text{Re}_x\text{Mo}_{1-x}\text{S}_2$, which was grown by chemical vapor deposition (CVD) under atmospheric pressure. The detailed material characterizations were performed using Raman spectroscopy, photoluminescence, and X-ray photoelectron spectroscopy (XPS) on an as-grown few-layer $\text{Re}_x\text{Mo}_{1-x}\text{S}_2$. The results show that both MoS_2 and ReS_2 peaks appear in the $\text{Re}_x\text{Mo}_{1-x}\text{S}_2$ Raman diagram. $\text{Re}_x\text{Mo}_{1-x}\text{S}_2$ is observed to emit light at a wavelength of 716.8 nm. The electronic band structure of the few layers of $\text{Re}_x\text{Mo}_{1-x}\text{S}_2$ calculated using the first-principles theory suggests that the band gap of $\text{Re}_x\text{Mo}_{1-x}\text{S}_2$ is larger than that of ReS_2 and smaller than that of MoS_2 , which is consistent with the photoluminescence results. The thermal stability of the few layers of $\text{Re}_x\text{Mo}_{1-x}\text{S}_2$ was evaluated using Raman temperature measurements. It is found that the thermal stability of $\text{Re}_x\text{Mo}_{1-x}\text{S}_2$ is close to those of pure ReS_2 and MoS_2 . The fabricated $\text{Re}_x\text{Mo}_{1-x}\text{S}_2$ photodetector shows a high response rate of 7.46 A W^{-1} under 365 nm illumination, offering a competitive performance to the devices based on TMDCs and graphenes. This study unambiguously distinguishes $\text{Re}_x\text{Mo}_{1-x}\text{S}_2$ as a future candidate in electronics and optoelectronics.

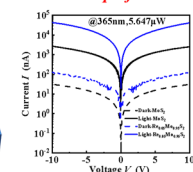
1. Synthesis method



2. 3D diagram of photodetector



3. Electrical performance



INTRODUCTION

Transition-metal dichalcogenides (TMDCs) are a semiconductor material with the general formula of MX_2 , where M is the transition metal atom of group VI or VII (e. g., Mo, Re, W) and X is the chalcogen atom (e.g., S, Se, Te). Due to their excellent optical and electrical properties, two-dimensional TMDCs are often applied to make a variety of logical devices.^{1–4} Molybdenum disulfide (MoS_2) is the most studied material in TMDCs. MoS_2 has a wide range of polymorphs, such as 1T, 2H, and 3R. The 2H structure of MoS_2 is thermodynamically stable, while the 3R phase is the metastable phase with the lowest energy. The 1T phase is the most unstable phase of the three types. Both 1T and 3R phases can be transformed into 2H phases at high temperatures.⁵ As a result, 2H- MoS_2 is a stable semiconductor. In the atomically thin monolayer limit, 2H- MoS_2 is a direct gap semiconductor with a band gap of about 1.9 eV. The band gap decreases from 1.9 to 0.7 eV for bulk with the increase in the number of MoS_2 layers, and MoS_2 is converted to an indirect semiconductor. To use MoS_2 in the construction of electronic devices, the performance of MoS_2 is often improved by adjusting the band gap. In particular, MoS_2 is doped/alloyed with other elements, mechanically strained, or stacked in the

form of heterostructures to achieve the tunable band gap.⁶ Among all these approaches, doping/alloying provides an easily scalable route to engineer the band structure.⁷

The two-dimensional ternary/quaternary materials synthesized by doping or alloying methods can alter the band gap compared with the intrinsic MoS_2 , manipulating traditional binary materials' optical and electrical properties.⁸ In addition to band gap modification, alloying can result in structural and electronic phase transformation. At the same time, alloying can also improve the thermodynamic stability of the material due to the increase in entropy. Current research indicates that Re- and W-doped MoS_2 are standard, such as $\text{Mo}_{1-x}\text{W}_x\text{S}_2$, $\text{Mo}_{1-x}\text{Re}_x\text{S}_2$.^{9,10} Due to the similar structure of WS_2 and MoS_2 , it is easy to form better doping and high alloying. In

Received: October 7, 2022

Accepted: November 28, 2022

Published: December 13, 2022



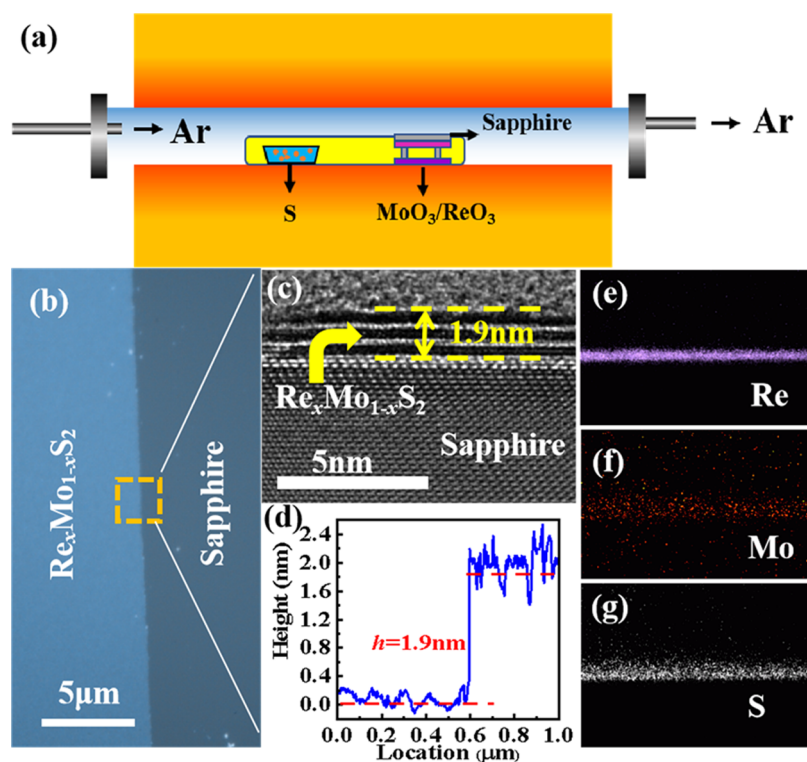


Figure 1. (a) Diagram of the CVD experimental device used in this work. (b) Optical image of a large-area continuous $\text{Re}_x\text{Mo}_{1-x}\text{S}_2$ thin film. (c) Cross-sectional projection electron microscopy image with a few layers of $\text{Re}_x\text{Mo}_{1-x}\text{S}_2$ /sapphire after 1.9 nm (TEM). (d) Thickness of the $\text{Re}_x\text{Mo}_{1-x}\text{S}_2$ film measured by AFM is 1.9 nm. (e–g) Energy-dispersive X-ray (EDX) mapping of the three elements of Re, Mo, and S.

contrast, ReS_2 (1T') and MoS_2 (2H) not only have different properties but also have very different phase structures and atomic structures. The atomic arrangement of the ReS_2 layer can be thought of as a distorted 1T arrangement and low in-plane crystal symmetry compared with MoS_2 . Therefore, ReS_2 and MoS_2 cannot be alloyed uniformly, resulting in no phase separation, which is not conducive to obtaining intrinsic properties and may degrade performance. Hence, obtaining high-performance $\text{Re}_x\text{Mo}_{1-x}\text{S}_2$ ternary materials is challenging, which are currently less studied.¹¹

In this work, few-layer $\text{Re}_x\text{Mo}_{1-x}\text{S}_2$ films were synthesized by the chemical vapor deposition (CVD) method using a certain proportion of sulfur, MoO_3 , and ReO_3 powders at a high temperature. Then, Raman spectroscopy and X-ray photoelectron spectroscopy (XPS) analysis of the resulting alloy materials were performed. To further study the optoelectronic properties of the synthesized $\text{Re}_x\text{Mo}_{1-x}\text{S}_2$, the structure of the ternary material was simulated, and the change of the band gap was calculated. A photodetector based on $\text{Re}_x\text{Mo}_{1-x}\text{S}_2$ was finally fabricated, which achieved high performance of photoresponse.¹² The synthesized material is still in the 2H phase, which has better stability than the 1T phase (MoS_2)_n cluster model.¹³ The present study offers a competitive performance to the devices based on TMDCs and graphenes, suggesting $\text{Re}_x\text{Mo}_{1-x}\text{S}_2$ as a future candidate in electronics and optoelectronics.

EXPERIMENT DETAILS

Growth of $\text{Re}_x\text{Mo}_{1-x}\text{S}_2$ and Preparation of Photodetectors. The CVD method (SK-G05123K-3-65S, Tianjin Zhonghuan Electric Furnace Co., Ltd., China) was used to prepare a few $\text{Re}_x\text{Mo}_{1-x}\text{S}_2$ films on sapphire substrates. Before

growth, the sapphire substrate was cleaned with ultrasonication, which included 10 min with acetone (CH_3COCH_3 , 99.5%), 5 min with isopropanol ($\text{C}_3\text{H}_8\text{O}$, 99.5%), and deionized water. Sulfur powder (0.7 g) was placed in the alumina combustion boat upstream of the quartz tubular furnace. Molybdenum trioxide powder (MoO_3 , 99.95%) and rhenium trioxide powder (ReO_3 , 99.95%) were evenly dispersed in the alumina crucible and placed in the center of the furnace. Then, the cleaned sapphire substrates were placed directly on top of the MoO_3 and ReO_3 powder alumina crucible boat. After the position was fixed, the gas was pumped by a vacuum pump, and argon gas was introduced. The repeated pumping cycles were carried out to remove the impurity gas in the furnace tube, and the reaction was further continued under optimized conditions in the Ar ambiance. Before the boat was heated, the pressure inside the chamber reached atmospheric pressure by flowing argon gas at a constant flow rate of 120 sccm. The growth temperature of $\text{Re}_x\text{Mo}_{1-x}\text{S}_2$ was then set to 850 °C and the holding time to 10 min. After the $\text{Re}_x\text{Mo}_{1-x}\text{S}_2$ film was grown, UV lithography (Suss MA6) and thermal evaporation coating (ASB-EPI-C6) were used to obtain 10 nm Cr and 50 nm Au on these samples.

Material and Electrical Properties. In this work, X-ray photoelectron spectroscopy (XPS) measurement was conducted using a VG ESCALAB 220i-XL system, which has a monochromatic $\text{Al K}\alpha$ (1486.6 eV) X-ray source and a 20 eV constant pass energy. The C 1s peak value of the core-level binding energy is 284.8 eV, which is used to eliminate the differential charging effect on the sample surface. Raman spectroscopy measurements were carried out in a confocal microscopy setup with a 514 nm solid-state green laser for excitation and a power of 0.15 mW. Transmission electron microscopy (TEM) was performed with America FEI-Titan Cubed Themis G2300, and the TEM information resolution

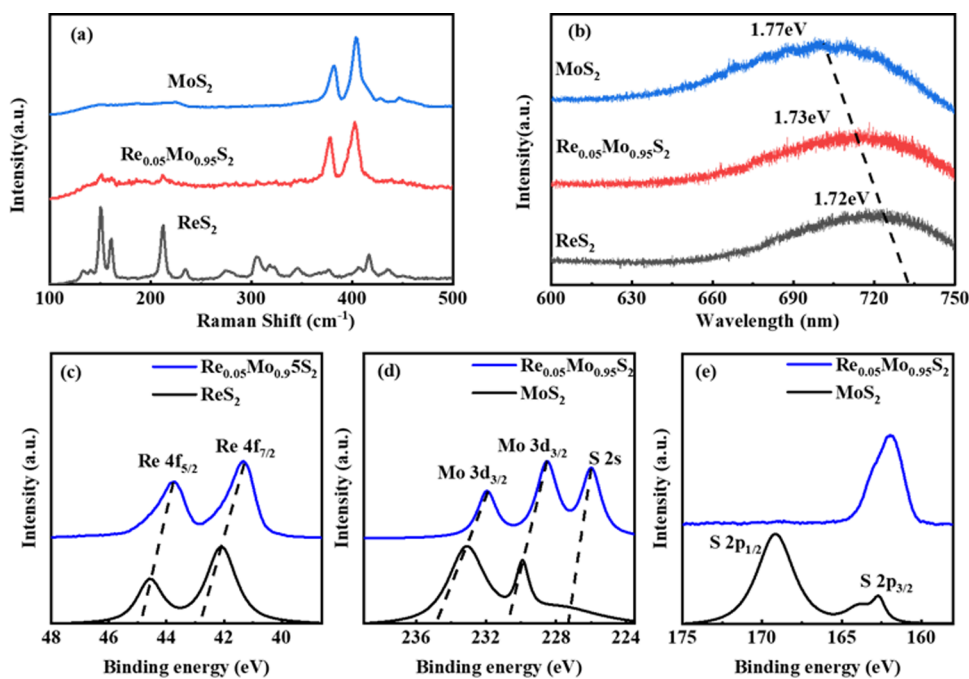


Figure 2. (a) Comparison of Raman signals of few layers of MoS_2 , $\text{Re}_{0.05}\text{Mo}_{0.95}\text{S}_2$, and ReS_2 . (b) Comparison of photoluminescence (PL) signals of a few layers of MoS_2 , $\text{Re}_{0.05}\text{Mo}_{0.95}\text{S}_2$, and ReS_2 . (c–e) Core-level XPS spectrum of Re 4f, Mo 3d, and S 2p of the multilayer $\text{Re}_{0.05}\text{Mo}_{0.95}\text{S}_2$ /sapphire sample.

(nonlinearity) was 0.06 nm. A Keithley 4200-SCS semiconductor analyzer was used to test the electrical characteristics of the corresponding photodetectors.

Theoretical Simulation. The first-principles calculations in density functional theory (DFT) were carried out by Cambridge Sequential Total Energy Package (CASTEP) using Generalized Gradient Approximation (GGA) in the Perdew–Burke–Ernzerhof (PBE) function for the structural optimization process.^{23,30} In the geometry optimization process, the final total energy change was less than 10^{-6} eV atom⁻¹, the maximum force on each atom in the crystal was less than 0.03 eV nm⁻¹, and the maximum stress of 0.03 eV nm⁻¹ was the convergence criterion. The maximum Hellmann–Feynman force was 0.05 eV Å⁻¹, which was sufficient to obtain a relaxed structure. Brillouin zone sampling adopts a $5 \times 5 \times 1$ Monkhorste–Pack grid. To ensure convergence, the electronic wave function was extended to a plane wave base with a cutoff value of 650 eV. Also, in the energy properties calculation process, the plane wave energy cutoff of 420 eV was used to calculate the energy band structure. For the sampling of the Brillouin zone of the body system, the structure optimization process and the energy band structure were calculated using $4 \times 4 \times 1$ point grids. At the same time, all calculations of structural relaxation were configured with a vacuum layer with a thickness of 20 Å on the *c*-axis.^{5,8,14}

RESULTS AND DISCUSSION

MoS_2 is a direct band gap in a single layer and an indirect band gap in a multilayer, while ReS_2 is a direct band gap in a single layer or a multilayer and will not change with the number of layers.¹³ MoS_2 is relatively stable in the 2H phase, while ReS_2 is relatively stable in the 1T' phase. In addition to the 2H phase, MoS_2 also has a metastable 1T' phase, it has a zero band gap and superior Weyl semimetal properties but is difficult to prepare. ReS_2 is extremely unstable in the 2H phase and has not been prepared yet.^{4–6,14} Few-layer $\text{Re}_x\text{Mo}_{1-x}\text{S}_2$ nanosheets were

synthesized on sapphire substrates in a chemical vapor deposition (CVD) furnace using ReO_3 and MoO_3 as the source materials (see the **Experiment Details** section). The schematic diagram of the CVD system is shown in **Figure 1a**. Weighed sulfur powder (0.7 g) was placed in a ceramic boat and placed in the first temperature zone of the tube furnace, which was upstream of the argon gas flow, and then MoO_3 (0.015 g) and ReO_3 (0.005 g) powders were put into the ceramic and placed in the second temperature zone of the tube furnace. The sapphire substrate was put on the top of the ceramic boat with the polished surface that needed to be used to deposit the thin film facing downward.¹⁵ **Figure 1b** shows the optical image of the large-area continuous $\text{Re}_x\text{Mo}_{1-x}\text{S}_2$ film. The cross-sectional TEM image of the film on the sapphire substrate is shown in **Figure 1c**, which indicates that the layers were a few layers of a thickness of about ~ 2 nm. The thickness of the grown $\text{Re}_x\text{Mo}_{1-x}\text{S}_2$ was measured using an atomic force microscope (AFM), and it is found to be about 1.9 nm. A single layer of two-dimensional material film was about 0.6 nm. The AFM result reveals that the grown $\text{Re}_x\text{Mo}_{1-x}\text{S}_2$ thin film had three layers, which proves that the large-area continuous thin film is multilayered, as described in ref 16. By adjusting the ratio of the precursors and the front and back positions of the precursors, a $\text{Re}_x\text{Mo}_{1-x}\text{S}_2$ film with *x* from 0 to 1 can be synthesized. As the value of *x* increases, the phase structure will change from the 2H phase to the 1T' phase. During the synthesis of $\text{Re}_x\text{Mo}_{1-x}\text{S}_2$, the bottleneck was the structural compatibility of these two monomers, since MoS_2 is the 2H phase while ReS_2 is the 1T' phase. Generally speaking, two materials with different phase structures will increase the entropy when forming an alloy, so the synthesis of $\text{Re}_x\text{Mo}_{1-x}\text{S}_2$ requires more energy than the original monomer.¹⁷ The low temperature cannot provide sufficient energy to meet the considerable formation energy of alloying required during growth. Fortunately, this problem can be effectively solved by increasing the growth temperature of the

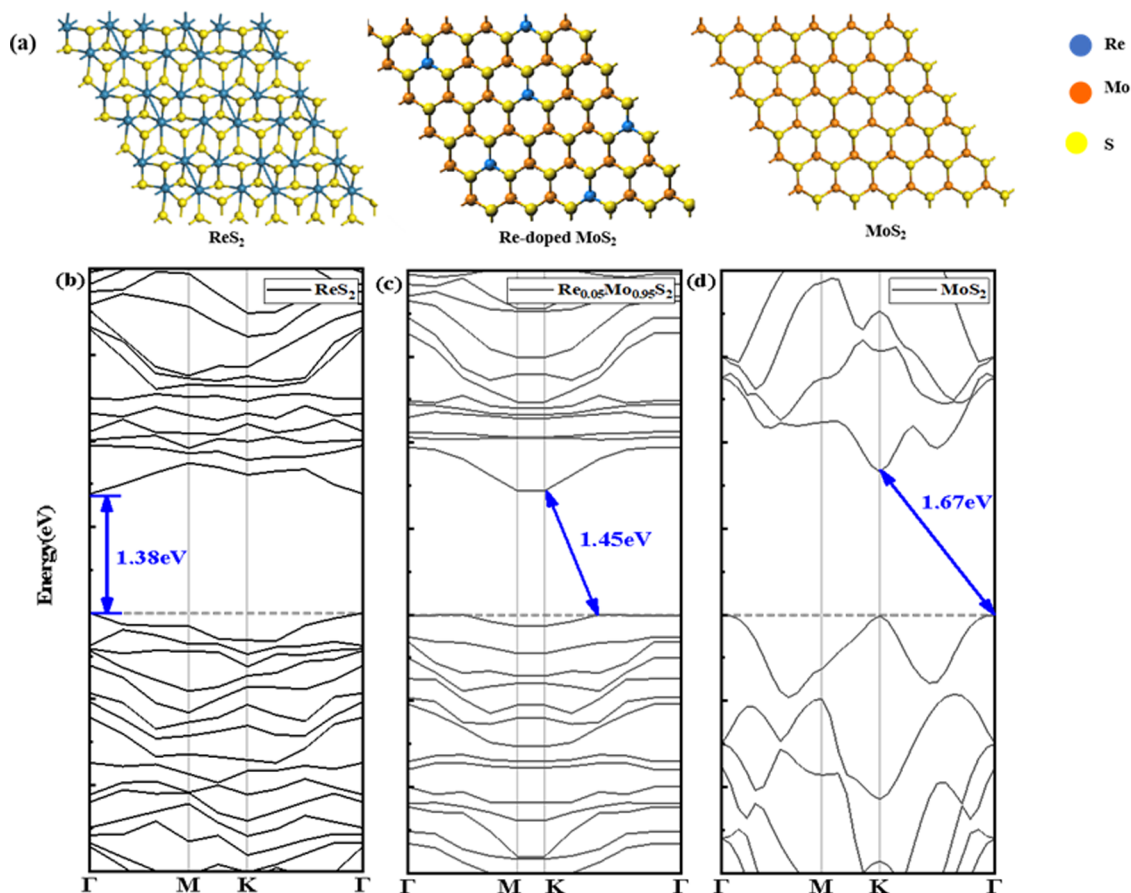


Figure 3. (a) Illustration of the three-dimensional (3D) drawing (purple symbol: W atoms; cyan symbol: Mo atoms; yellow symbol: S atoms) of ReS_2 , $\text{Re}_x\text{Mo}_{1-x}\text{S}_2$, and MoS_2 layers, in which Mo and Re elements are spatially segregated. Electronic band structure of (b) three-layer ReS_2 , (c) three-layer $\text{Re}_{0.05}\text{Mo}_{0.95}\text{S}_2$, and (d) three-layer MoS_2 .

$\text{Re}_x\text{Mo}_{1-x}\text{S}_2$ alloy.¹⁸ Increasing the growth temperature can provide enough energy to overcome the large energy barrier and form a uniform phase (1T' or 2H) structure¹⁹ and the composition of the $\text{Re}_x\text{Mo}_{1-x}\text{S}_2$ alloy. To further observe the thickness and number of layers of $\text{Re}_x\text{Mo}_{1-x}\text{S}_2$, the TEM image of the $\text{Re}_x\text{Mo}_{1-x}\text{S}_2$ film was taken. As shown in Figure 1c, it can be observed that the thickness of the $\text{Re}_x\text{Mo}_{1-x}\text{S}_2$ film is about 1.9 nm, with three layers in total,²⁰ which is consistent with the results measured by AFM (Supporting Information S1). To further verify Re, Mo, and S in the $\text{Re}_x\text{Mo}_{1-x}\text{S}_2$ film, energy-dispersive X-ray (EDX) mapping was performed. The results are shown in Figure 1d–f. The three elements of Re, Mo, and S shown in Figure 1e–g are purple, red, and gray, respectively. These three elements are not uniform in our synthesized film, and the spatial segregation of various elements can be seen in the figure.²¹

In addition, Raman spectroscopy was performed to characterize the composition-dependent lattice vibration mode of the $\text{Re}_x\text{Mo}_{1-x}\text{S}_2$ film. Figure 2a shows its four different vibration modes. For pure MoS_2 , the two characteristic peaks of the E_{2g} and A_{1g} modes are located at 382 and 403 cm^{-1} , respectively, while the two characteristic peaks E_{2g} and A_{1g} of pure ReS_2 are located at 151 and 213 cm^{-1} , respectively. When $\text{Re}_x\text{Mo}_{1-x}\text{S}_2$ is in the 1T' phase, it will mainly appear as the peak of ReS_2 , and when $\text{Re}_x\text{Mo}_{1-x}\text{S}_2$ is in the 2H phase, it will mostly show MoS_2 peaks, which are attributed to the E_{2g} and A_{1g} modes of MoS_2 . In addition, other peaks at 152 and 214 cm^{-1} indicate the 2H phase of $\text{Re}_x\text{Mo}_{1-x}\text{S}_2$. These two Raman peaks should be due to Re

doping activating a new vibration mode caused by the phonon momentum with a large wave vector. The increase of the doping concentration makes the intensity of the Raman peaks of the 2H and 1T' phase alloys weaker, and the widening of the full width at half-maximum (FWHM) is due to the softening or reforming of phonons caused by the enhancement of the electron–phonon coupling effect. Compared with pure MoS_2 , the E_g and A_g vibration modes at $\text{Re}_x\text{Mo}_{1-x}\text{S}_2$ move to lower wavenumbers. E_g is shifted to the left by 4 cm^{-1} , and A_g is shifted to the left by 1 cm^{-1} , causing the mode peak separation from the original of 21 cm^{-1} to increase to 24 cm^{-1} . Compared with pure ReS_2 , the E_g -like and A_g -like vibration modes at 151 and 213 cm^{-1} change little, respectively, but the FWHM widens. This is because the main body or most atoms of $\text{Re}_x\text{Mo}_{1-x}\text{S}_2$ are still Re. The broadening is due to alloy scattering or doping of Mo atoms.²² The hardening of the A_g mode of $\text{Re}_x\text{Mo}_{1-x}\text{S}_2$ may be due to changes in the bonding environment of S atoms. Based on the results obtained from the above Raman spectroscopy, the dependence of the phase structure of the prepared alloy material on the composition change is confirmed, and the preliminary analysis of the $\text{Re}_x\text{Mo}_{1-x}\text{S}_2$ gold composition using the Raman test is possible.²³ The Raman data of ReS_2 , $\text{Re}_x\text{Mo}_{1-x}\text{S}_2$, and MoS_2 are distinguished, proving that Re and Mo atoms diffuse each other and form bonds and synthesize the $\text{Re}_x\text{Mo}_{1-x}\text{S}_2$ ternary alloy. The photoluminescence of $\text{Re}_x\text{Mo}_{1-x}\text{S}_2$ in Figure 2b indicates adjustable band gaps of 1.77–1.72 eV in these three materials. The peak positions of the pure few-layer ReS_2 , few-layer $\text{Re}_x\text{Mo}_{1-x}\text{S}_2$, and pure few-layer MoS_2 are about 721, 717,

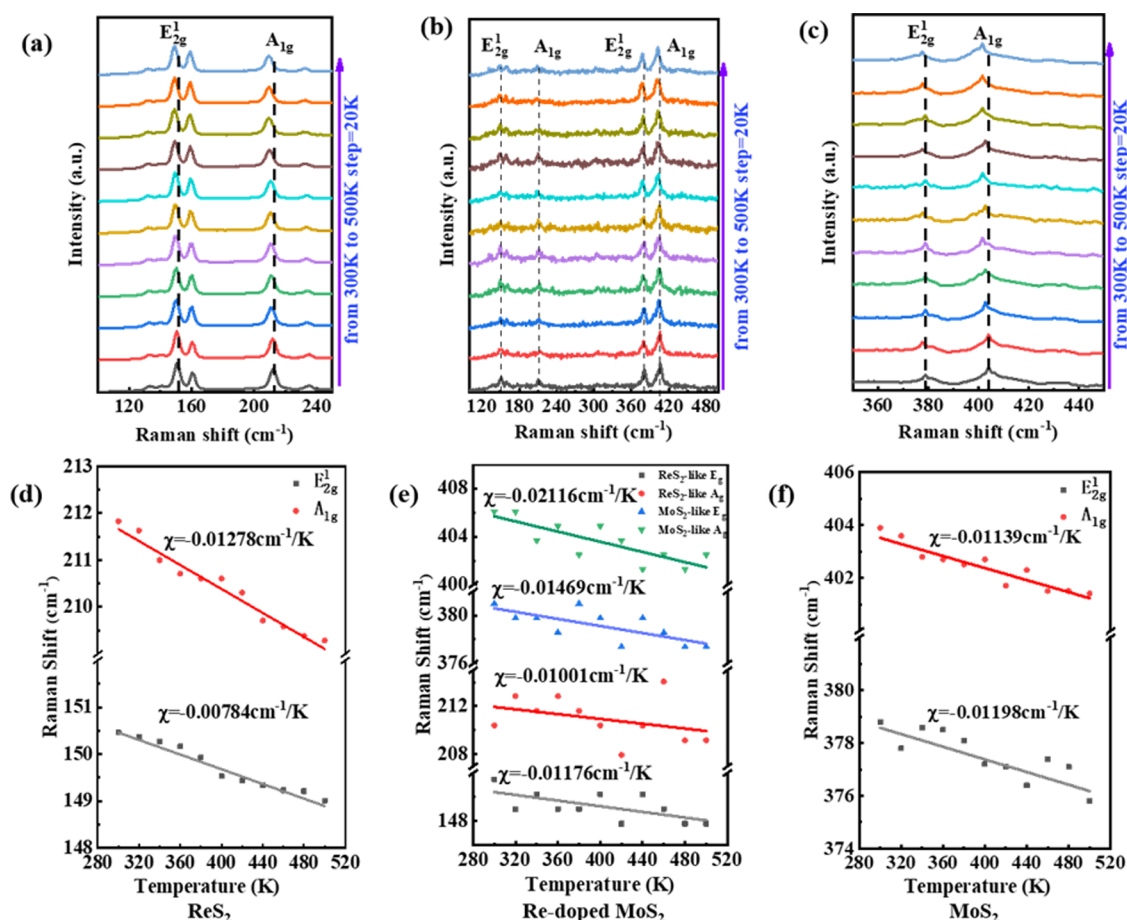


Figure 4. Temperature-dependent Raman spectra. (a) Sample ReS_2 , (b) $\text{Re}_{0.05}\text{Mo}_{0.95}\text{S}_2$, and (c) MoS_2 . The Raman shift of each mode as a function for temperature (d–f), including the value of χ obtained from linear fitting.

and 700 nm, respectively. The calculated band gaps are 1.72, 1.73, and 1.77 eV, respectively. The measured results are consistent with the narrowing of the band gap caused by Re doping achieved by the first-principles calculations.²⁴ The exact composition of the alloy samples was confirmed and their preliminarily electronic structures were preliminarily analyzed based on the XPS data.²⁵ In pure MoS_2 , Mo 3d core-level binding energy peaks (Figure 2d) are observed at 232.9 and 229.8 eV, corresponding to Mo 3d_{3/2} and Mo 3d_{5/2} peaks. After doping Re into 2H- MoS_2 , Mo 3d_{3/2} transitions from 232.9 to 233.4 eV and Mo 3d_{5/2} transitions from 229.8 to 230.2 eV, indicating the upward movement of E_F in the conduction band and the n-type doping in the MoS_2 crystal. In pure ReS_2 , Re 4f core-level binding energy peaks were observed at 44.8 and 42.3 eV (Figure 2c), corresponding to the Re 4f_{5/2} and Re 4f_{7/2} peaks. It is worth noting that after doping Mo into 1T'- ReS_2 , Re 4f_{5/2} changed from 44.8 to 43.6 eV and Re 4f_{7/2} changed from 42.3 to 41.1 eV, indicating that E_F moved down to the valence band and the p-type-doped crystals in ReS_2 .²⁶ This doping-induced binding energy shift is also reflected in the S 2p core-level binding energy peak (Figure 2e), where obvious mutations and phase transitions are observed. As shown in Figure 1a, the downward shift of E_F of the 1T' alloy and the upward shift of the 2H alloy are because the d-orbital of the Re element has one more valence electron than the Mo element.²⁷ In addition, the movement of E_F indicates that the effective modulation and doping effect of the electronic structure of these alloys are atomic substitution rather than physical adsorption.²⁸

Figure 3a shows the structure diagram of the three materials. It can be seen that $\text{Re}_x\text{Mo}_{1-x}\text{S}_2$ is different from the original atomic arrangement. Here, the first principles in density functional theory (DFT) were used to study the three-layer MoS_2 , the three-layer $\text{Re}_x\text{Mo}_{1-x}\text{S}_2$, and the three-layer ReS_2 , so the total energy program is calculated from scratch using Cambridge Sequential Total Energy Package (CASTEP).^{20,29} The direct gap between the three-layer MoS_2 , the three-layer $\text{Re}_x\text{Mo}_{1-x}\text{S}_2$, and ReS_2 has been pointed out. The calculated result was the same as the trend shown in Figure 2b, which shows that due to the doping of elements, the band gap adjustment of the semiconductor film can be realized, proving the present calculation's accuracy.⁵

Figure 4a–c shows the effect of temperature changes on the E_g and A_g Raman modes of the few layers of ReS_2 , $\text{Re}_x\text{Mo}_{1-x}\text{S}_2$, and MoS_2 . These three materials were measured in the range of 300–500 K with a 325 nm excitation laser based on the Grüneisen model to fit the relationship between the peak position of the E_g and A_g modes and the temperature

$$\omega(T) = \omega_0 + xT \quad (1)$$

where ω_0 is the temperature at the peak position of the Raman mode at 0 K and x is the first-order temperature of the same mode coefficient.⁶ The slope of the fitted line gives the first-order temperature coefficient of the specific Raman mode. As shown in Figure 4d, the first-order temperature coefficient x of the A_{1g} and E_{2g}^1 modes of pure ReS_2 are -0.01278 and -0.00784 $\text{cm}^{-1} \text{K}^{-1}$, respectively. As shown in Figure 4e, the first-order

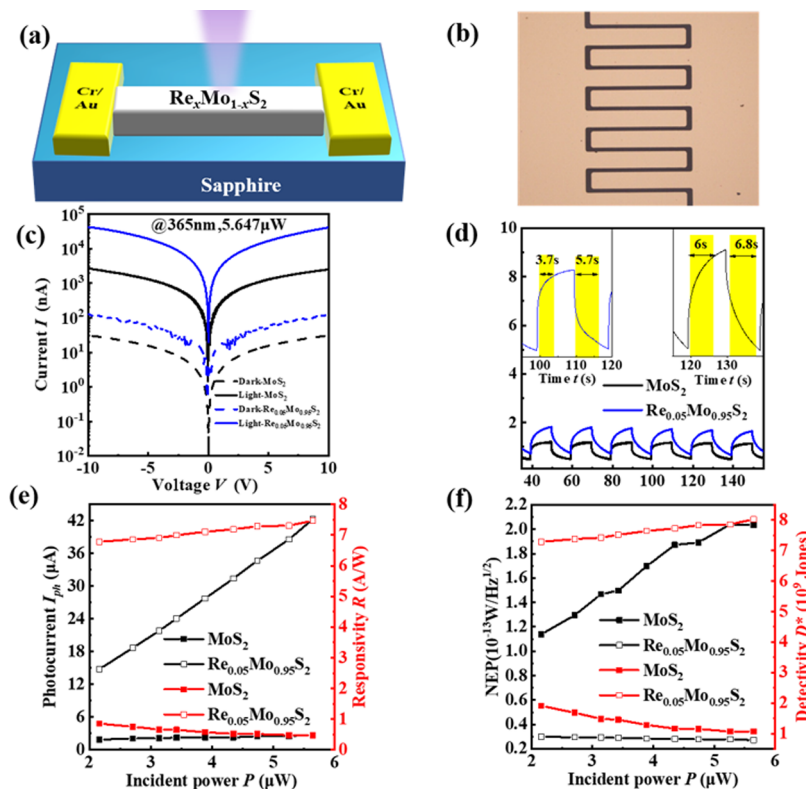


Figure 5. (a) 3D schematic diagram of the $\text{Re}_x\text{Mo}_{1-x}\text{S}_2/\text{sapphire}$ photodetector, where the electrodes are Cr/Au. (b) Optical micrograph of the $\text{Re}_x\text{Mo}_{1-x}\text{S}_2/\text{sapphire}$ photodetector. (c) Optical response characteristics of the $\text{Re}_x\text{Mo}_{1-x}\text{S}_2/\text{sapphire}$ and the $\text{MoS}_2/\text{sapphire}$ photodetector as a function of voltage under 365 nm laser irradiation. Response time of $\text{Re}_x\text{Mo}_{1-x}\text{S}_2/\text{sapphire}$ and $\text{MoS}_2/\text{sapphire}$ photodetectors under 10 V illumination and 365 nm laser irradiation, photocurrent (I_{ph}), responsivity (R), and noise equivalent power (NEP) at these three wavelengths. The noise-specific detection rates (D^*) below correspond to (d)–(f).

temperature coefficient α of ReS_2 -like E_{g} and ReS_2 -like A_{g} modes of $\text{Re}_x\text{Mo}_{1-x}\text{S}_2$ are -0.01176 and $-0.01001 \text{ cm}^{-1} \text{ K}^{-1}$, respectively. The first-order temperature coefficient α of MoS_2 -like E_{g} and MoS_2 -like A_{g} modes of $\text{Re}_x\text{Mo}_{1-x}\text{S}_2$ are -0.01496 and $-0.02116 \text{ cm}^{-1} \text{ K}^{-1}$, respectively. As shown in Figure 4f, the first-order temperature coefficient α of pure MoS_2 in $A_{1\text{g}}$ and $E_{2\text{g}}$ modes is -0.01139 and $-0.01198 \text{ cm}^{-1} \text{ K}^{-1}$, respectively. In contrast, nondoped compounds have higher thermal stability due to the greater free and internal energy of the ternary $\text{Re}_x\text{Mo}_{1-x}\text{S}_2$ alloy. The opaque photodetector array with Cr/Au as the electrode was fabricated on $\text{Re}_{0.05}\text{Mo}_{0.95}\text{S}_2/\text{sapphire}$ ($1 \times 1 \text{ cm}^2$) by semiconductor processing technology, and the $\text{MoS}_2/\text{sapphire}$ photodetector used as a control was fabricated using the same process.

The 3D schematic diagram of the $\text{Re}_{0.05}\text{Mo}_{0.95}\text{S}_2/\text{sapphire}$ photodetector is shown in Figure 5a, where the thickness of the electrode (Cr/Au) on the device is 10/50 nm, and the effective area of each device array is $47\,376 \mu\text{m}^2$. Meanwhile, Figure 5a shows the device structure of the $\text{Re}_{0.05}\text{Mo}_{0.95}\text{S}_2/\text{sapphire}$ Schottky junction-based UV photodetector. Using the above method, a two-dimensional (2D) $\text{Re}_{0.05}\text{Mo}_{0.95}\text{S}_2$ layer was in situ van der Waals epitaxy grown on a sapphire substrate to form a Schottky junction, which is beneficial to constructing high-quality Schottky junction and effectively reducing the interface defects introduced by the wet transfer process. Figure 5b shows the optical picture of a single device. Figure 5c plots the current–voltage (I – V) curves of the Schottky junction in darkness and 365 nm light. The device exhibits prominent photovoltaic characteristics, enabling the photodetector to operate in the self-driven mode. The significant enhancement

of reverse current under UV irradiation can be attributed to two aspects: (i) the reduction of the Schottky barrier under UV irradiation will result in a large photocurrent under reverse bias and (ii) the multiplier gain may be caused by carrier scattering in the $\text{Re}_{0.05}\text{Mo}_{0.95}\text{S}_2$ layer. Figure 5c shows the dark current (I_{dark}) and photocurrent (I_{light}) of the two devices ($\text{Re}_{0.05}\text{Mo}_{0.95}\text{S}_2$ and MoS_2) as a function of the bias voltage under 365 nm laser irradiation. I_{dark} is the current generated by the device under the bias voltage when there is no incident laser and I_{light} is the current generated by the device under the bias voltage and incident laser irradiation.³¹ The dark current of the $\text{Re}_{0.05}\text{Mo}_{0.95}\text{S}_2$ device is 128 nA at 10 V, while the dark current of the MoS_2 device is only 29.7 nA, which may be attributed to the smaller band gap and the lower potential barrier of the $\text{Re}_{0.05}\text{Mo}_{0.95}\text{S}_2$ device due to the doping of the Re element. At the same time, under 10 V and 365 nm (5.647 μW) illumination, the photocurrent of the device increased from 2734 nA (MoS_2) to 42 288 nA ($\text{Re}_{0.05}\text{Mo}_{0.95}\text{S}_2$), and the $I_{\text{light}}/I_{\text{dark}}$ ratio of the $\text{Re}_{0.05}\text{Mo}_{0.95}\text{S}_2$ device increased by 3.62 times. This can be explained by the fact that the light scattering caused by the $\text{Re}_{0.05}\text{Mo}_{0.95}\text{S}_2$ structure is stronger than that of MoS_2 , and the band gap is reduced due to local strain, which leads to an increase in the mobility of photogenerated carriers. Further observation of the improvement of the device through the performance of the $\text{Re}_{0.05}\text{Mo}_{0.95}\text{S}_2$ structure, the response time of two photodetectors (MoS_2 and $\text{Re}_{0.05}\text{Mo}_{0.95}\text{S}_2$) was also studied. Figure 5d shows that the photocurrent of the two devices periodically changes as the 365 nm laser was turned on/off at a voltage of 10 V, whereas the 365 nm (5.647 μW) laser was turned on/off every 20 s. Both devices show stable switching characteristics, and the photocurrent observed in the

Re_{0.05}Mo_{0.95}S₂/sapphire photodetector is more significant than that in the MoS₂/sapphire photodetector. Figure 5d defines the rise time (t_{rise}) and the fall time (t_{fall}) of the two devices under 365 nm laser and 4 V bias irradiation. Here, the rise time of the device can be obtained by calculating the time required for the photocurrent to increase from 10% of the maximum photocurrent to 90% under illumination. The fall time is defined as the photocurrent falling from 10% of the maximum photocurrent to 90%.

Comparing the two devices, it can be observed that the rise time is reduced from 6 s (MoS₂) to 3.7 s (Re_{0.05}Mo_{0.95}S₂), and the fall time is decreased from 6.8 s (MoS₂) to 5.7 s (Re_{0.05}Mo_{0.95}S₂). The shortened rise and fall times may be due to a decrease in effective electron quality and an increase in electron mobility. In addition, the photocurrent (I_{ph}) is one of the parameters reflecting the light response of the photodetector, which can be calculated using the below formula

$$I_{\text{ph}} = I_{\text{light}} - I_{\text{dark}} \quad (2)$$

where I_{light} and I_{dark} have been defined in Figure 5c.²⁹ The responsivity (R) is a significant indicator to measure the photoelectric conversion characteristics and photoelectric conversion spectrum of a photodetector and can be calculated by the below formula

$$R = I_{\text{ph}} / (P_i \times S) \quad (3)$$

where I_{ph} is the photocurrent and S and P_i are the active area of the film and the power density of the incident laser, respectively.^{32,33} Figure 5e shows the relationship between the I_{ph} and R of the photodetector based on MoS₂ and Re_{0.05}Mo_{0.95}S₂ at the incident wavelength of 365 nm light and the different incident power at 10 V voltage. It can be found that under the irradiation of three wavelengths, the Re_{0.05}Mo_{0.95}S₂ device shows a higher photocurrent and responsivity than the MoS₂ device. The maximum responsivity of the device under a 365 nm incident laser was increased from 0.85 A W⁻¹ (MoS₂) to 7.46 A W⁻¹ (Re_{0.05}Mo_{0.95}S₂). In particular, the relationship between responsivity and different incident powers is studied. The responsivity reaches a peak first and then decreases as the incident power increases.

This may be due to the saturation of trap states at the interface, as well as the low recombination frequency and long carrier lifetime of low-power lasers. To further observe the improvement of the device performance by the Re_{0.05}Mo_{0.95}S₂ material, the noise equivalent power (NEP) and specific detection rate (D^*) at different incident powers were calculated. NEP can quantitatively calculate the signal-to-noise ratio, defined as the excitation power required to generate a signal equal to the noise level in a 1 Hz bandwidth. It can be calculated using the below formula

$$\text{NEP} = \sqrt{2qI_{\text{dark}}\Delta f} / R \quad (4)$$

where I_{dark} and R are the dark current and responsivity, respectively, and Δf is the bandwidth (Δf is defined as 1 in this article).²⁰ The dark current excitation noise is the main contribution to the total noise of the photodetector. D^* can be calculated using the below formula

$$D^* = A^{1/2} / \text{NEP} \quad (5)$$

where A is the active area of the MoS₂ film under the incident laser irradiation. Figure 5f contains the relationship between the NEP and D^* of the photodetector based on MoS₂ and

Re_{0.05}Mo_{0.95}S₂ and the different incident power at a wavelength of 365 nm and a voltage of 10 V.²⁸ As it is well-known, the larger the D^* value, the smaller the NEP value can be, which means that the noise of the device is lower and the detection capability is stronger. In contrast, the decrease in NEP and increase in D^* of the Re_{0.05}Mo_{0.95}S₂ photodetector under the irradiation of three different incident lasers indicate that the Re_{0.05}Mo_{0.95}S₂ material can significantly improve the photo-detection compared with the weak growth in the dark current. Table 1 summarizes some of the reported performance parameters of photodetectors, showing the photocurrent of the detector, which has a stronger detection ability.

Table 1. Comparison of the Critical Parameters of Our Device to the Reported 2D Material-Based Photodetectors

photodetector	R [A/W]	D^* [Jones]	response time [s]	refs
Re _x Mo _{1-x} S ₂ /sapphire	7.46	8.0×10^9	3.70	this work
MoS ₂ /sapphire	0.85	1.9×10^9	6.0	this work
MoS ₂ /glass	0.032	1.0×10^9		34
MoS ₂ /SiO ₂	0.048	1.3×10^7		35
MoS ₂ /SiC	0.25	5.6×10^8	2.19	36
ReS ₂ (1-x)Se _{2x} /SiO ₂	0.25		0.015	37
MoS ₂ /PSS	0.032	1.2×10^{10}	2.24	38
MoS ₂ /PGS	0.25	5.6×10^8	2.19	39
MoS ₂ /sapphire	0.071		0.50	40
MoS ₂ (1-x)Se _{2x} /SiO ₂	2.5×10^{-4}		0.038	41

CONCLUSIONS

In conclusion, this study has demonstrated that the few-layer Re_xMo_{1-x}S₂ films were synthesized by the CVD method at 1 atm pressure and that the high-performance photodetector has been successfully constructed on the as-prepared Re_xMo_{1-x}S₂ on a sapphire substrate.⁴² The Raman, PL, and XPS measurements have been performed on the as-grown Re_xMo_{1-x}S₂ few layers to understand film quality. The results show that both MoS₂ and ReS₂ peaks appear in the Re_xMo_{1-x}S₂ Raman diagram. Re_xMo_{1-x}S₂ is observed to emit light at a wavelength of 716.8 nm. The electronic band structure of the few-layer Re_xMo_{1-x}S₂ is calculated using the first-principles theory, demonstrating that the band gap of Re_xMo_{1-x}S₂ is larger than that of ReS₂ and smaller than that of MoS₂, which is consistent with the photoluminescence results. Temperature-dependent Raman spectroscopy on ReS₂, Re_{0.05}Mo_{0.95}S₂, and MoS₂ layers have been carried out for the purpose of comparative study, and further, the thermal stability of the few layers of Re_xMo_{1-x}S₂ has been evaluated. It was found that the thermal stability of Re_xMo_{1-x}S₂ is close to that of pure ReS₂ and MoS₂. The manufactured Re_xMo_{1-x}S₂ photodetector shows superiority to the pure MoS₂ detector, with a higher responsivity of 7.46 A W⁻¹. Our results provide a positive prospect for further improving the performance of the few-layer Re_{0.05}Mo_{0.95}S₂ photodetector.

ASSOCIATED CONTENT

Supporting Information

The Supporting Information is available free of charge at <https://pubs.acs.org/doi/10.1021/acsomega.2c06480>.

AFM image of Re_xMo_{1-x}S₂ (PDF)

AUTHOR INFORMATION

Corresponding Author

Shuangwu Huang – College of Materials Science and Engineering, College of Electronic and Information Engineering, Institute of Microelectronics (IME), Guangdong Research Center for Interfacial Engineering of Functional Materials, Shenzhen University, Shenzhen 518060, People's Republic of China; orcid.org/0000-0002-1980-4979; Email: mark_huang@szu.edu.cn

Authors

Xinke Liu – College of Materials Science and Engineering, College of Electronic and Information Engineering, Institute of Microelectronics (IME), Guangdong Research Center for Interfacial Engineering of Functional Materials, Shenzhen University, Shenzhen 518060, People's Republic of China; orcid.org/0000-0002-3472-5945

Jiangchuan Wang – College of Materials Science and Engineering, College of Electronic and Information Engineering, Institute of Microelectronics (IME), Guangdong Research Center for Interfacial Engineering of Functional Materials, Shenzhen University, Shenzhen 518060, People's Republic of China

Yuheng Lin – College of Materials Science and Engineering, College of Electronic and Information Engineering, Institute of Microelectronics (IME), Guangdong Research Center for Interfacial Engineering of Functional Materials, Shenzhen University, Shenzhen 518060, People's Republic of China

Jie Zhou – College of Materials Science and Engineering, College of Electronic and Information Engineering, Institute of Microelectronics (IME), Guangdong Research Center for Interfacial Engineering of Functional Materials, Shenzhen University, Shenzhen 518060, People's Republic of China

Qiang Liu – State Key Laboratory of Functional Materials for Informatics, Shanghai Institute of Microsystem and Information Technology, CAS, Shanghai 200050, People's Republic of China

Wenjie Yu – State Key Laboratory of Functional Materials for Informatics, Shanghai Institute of Microsystem and Information Technology, CAS, Shanghai 200050, People's Republic of China

Yongqing Cai – Joint Key Laboratory of Ministry of Education, Institute of Applied Physics and Materials Engineering, University of Macau, Macau 999078, China; orcid.org/0000-0002-3565-574X

Xiaohua Li – College of Materials Science and Engineering, College of Electronic and Information Engineering, Institute of Microelectronics (IME), Guangdong Research Center for Interfacial Engineering of Functional Materials, Shenzhen University, Shenzhen 518060, People's Republic of China

V. Divakar Botcha – College of Materials Science and Engineering, College of Electronic and Information Engineering, Institute of Microelectronics (IME), Guangdong Research Center for Interfacial Engineering of Functional Materials, Shenzhen University, Shenzhen 518060, People's Republic of China

Tingke Rao – College of Materials Science and Engineering, College of Electronic and Information Engineering, Institute of Microelectronics (IME), Guangdong Research Center for Interfacial Engineering of Functional Materials, Shenzhen University, Shenzhen 518060, People's Republic of China

Complete contact information is available at:
<https://pubs.acs.org/10.1021/acsomega.2c06480>

Notes

The authors declare no competing financial interest.

ACKNOWLEDGMENTS

This work was supported by the National Key Research and Development Program of China (2017YFB0403000), the National Natural Science Foundation of China (61974144), the Guangdong Province Key Research and Development Plan (2020B010174003), the Science and Technology Foundation of Shenzhen (JSGG20191129114216474), the Science and Technology Project of Shenzhen City (JSGG20110802154213040 and JSGG20201102152403008), and the Project of Innovation and Strong School (PT2020C002). The authors wish to acknowledge the assistance on HRTEM observation received from the Electron Microscope Center of Shenzhen University and the device fabrication process in the Photonics Center of Shenzhen University. The sulfur powder was provided by Xintai Wenhe Chemical Pte Ltd. (China, Shandong). The CVD system (CVD-12IIIH-3Z/G) was provided by Tianjin Zhonghuan Furnace Corp. The Open Project of State Key Laboratory of Functional Materials for Informatic.

REFERENCES

- (1) Du, H.; Zhang, Q. P.; Zhao, B.; Marken, F.; Gao, Q. C.; Lu, H.-X.; Guan, L.; Wang, H.-L.; Shao, G.; Xu, H.-L.; Zhang, R.; Fan, B.-B. Novel hierarchical structure of MoS₂/TiO₂/Ti₃C₂Tx composites for dramatically enhanced electromagnetic absorbing properties. *J. Adv. Ceram.* **2021**, *10*, 1042–1051.
- (2) Wu, M.; He, Y.; Wang, L.-B.; Xia, Q.-X.; Zhou, A.-G. Synthesis and electrochemical properties of V₂C MXene by etching in opened/closed environments. *J. Adv. Ceram.* **2020**, *9*, 749–758.
- (3) Xu, Q.; Zhou, Y.-C.; Zhang, H.-M.; Jiang, A.-N.; Tao, Q.-Z.; Lu, J.; Rosen, J.; Niu, Y.-H.; Grasso, S.; Hu, C.-F. Theoretical prediction, synthesis, and crystal structure determination of new MAX phase compound V₂SnC. *J. Adv. Ceram.* **2020**, *9*, 481–492.
- (4) Gao, J.; Kim, Y.-D.; Liang, L.-B.; Idrobo, J.-C.; Chow, P.; Tan, J.-W.; Li, B.-C.; Li, L.; Sumpster, B.-G.; Lu, T.-M.; Meunier, V.; Hone, J.; Koratkar, N. Transition-Metal Substitution Doping in Synthetic Atomically Thin Semiconductors. *Adv. Mater.* **2016**, *28*, 9735–9743.
- (5) Deng, Q.-X.; Li, X.-B.; Si, H.-Y.; Hong, J.-H.; Wang, S.-Y.; Feng, Q.-L.; Hu, C.-X.; Wang, S.-S.; Zhang, H.-L.; Suenaga, K.; Xu, H. Strong Band Bowing Effects and Distinctive Optoelectronic Properties of 2H and 1T' Phase-Tunable Mo_(x)Re_(1-x)(S₂)Alloys. *Adv. Funct. Mater.* **2020**, *30*, No. 2003264.
- (6) Ding, Y.-H.; Cheng, Z.; Zhu, X.-L.; Yvind, K.; Dong, J.-J.; Galili, M.; Hu, H.; Mortensen, N.-A.; Xiao, S.-S.; Oxenlowe, L.-K. Ultra-compact integrated graphene plasmonic photodetector with bandwidth above 110 GHz. *Nanophotonics* **2020**, *9*, 317–325.
- (7) Hafeez, M.; Gan, L.; Li, H.-Q.; Ma, Y.; Zhai, T.-Y. Large-Area Bilayer ReS₂ Film/Multilayer ReS₂ Flakes Synthesized by Chemical Vapor Deposition for High Performance Photodetectors. *Adv. Funct. Mater.* **2017**, *26*, 4551–4560.
- (8) Liang, Q.-J.; Wang, Q.-X.; Zhang, Q.; Wei, J.-X.; Lim, S.; Zhu, R.; Hu, J.-X.; Wei, W.; Lee, C.; Sow, C.; Zhang, W.-J.; Wee, A. High-Performance, Room Temperature, Ultra-Broadband Photodetectors Based on Air-Stable PdSe₂. *Adv. Mater.* **2019**, *31*, No. 1807609.
- (9) Chow, P. C. Y.; Someya, T. Organic Photodetectors for Next-Generation Wearable Electronics. *Adv. Mater.* **2020**, *32*, No. 1902045.
- (10) Hu, P.-A.; Wen, Z.-Z.; Wang, L.-F.; Tan, P.-H.; Xiao, K. Synthesis of Few-Layer GaSe Nanosheets for High Performance Photodetectors. *ACS Nano* **2012**, *6*, 5988–5994.
- (11) Li, X.-B.; Cui, F.-F.; Feng, Q.-L.; Wang, G.; Xu, X.-S.; Wu, J.-X.; Mao, N.-N.; Liang, X.; Zhang, Z.-Y.; Zhang, J.; Xu, H. Controlled growth of large-area anisotropic ReS₂ atomic layer and its photodetector application. *Nanoscale* **2016**, *8*, 18956–18962.

- (12) Liu, X.-K.; Wu, J.; Yu, W.-J.; Chen, L.; Huang, Z.-H.; Jiang, H.; He, J.-Z.; Liu, Q.; Lu, Y.-M.; Zhu, D.-L.; Liu, W.-J.; Cao, P.-J.; Han, S.; Xiong, X.-B.; Xu, W.-Y.; Ao, J.-P.; Ang, K.-W.; He, Z.-B. Monolayer $W_xMo_{1-x}S_2$ Grown by Atmospheric Pressure Chemical Vapor Deposition: Bandgap Engineering and Field Effect Transistors. *Adv. Funct. Mater.* **2017**, *27*, No. 1606469.
- (13) Wang, Y.-Y.; Deng, J.-J.; Wang, X.; Che, J.-T.; Ding, X.-L. Small stoichiometric $(MoS_2)_n$ clusters with the 1T phase. *Phys. Chem. Chem. Phys.* **2018**, *20*, 6365–6373.
- (14) Zhang, K.-H.; Bersch, B.-M.; Joshi, J.; Addou, R.; Cormier, C.-R.; Zhang, C.-X.; Xu, K.; Briggs, N.-C.; Wang, K.; Subramanian, S.; Cho, K.; Fullerton-Shirey, S.; Wallace, R. M.; Vora, P. M.; Robinson, J. A. Tuning the Electronic and Photonic Properties of Monolayer MoS_2 via In Situ Rhenium Substitutional Doping. *Adv. Funct. Mater.* **2018**, *28*, No. 1706950.
- (15) Butanovs, E.; Kuzmin, A.; Piskunov, S.; Smits, K.; Kalinko, A.; Polyakov, B. Synthesis and characterization of GaN/ReS_2 , ZnS/ReS_2 and ZnO/ReS_2 core/shell nanowire heterostructures. *Appl. Surf. Sci.* **2021**, *536*, No. 147841.
- (16) Cui, F.-F.; Li, X.-B.; Feng, Q.-L.; Yin, J.-B.; Zhou, L.; Liu, D.-Y.; Liu, K.-Q.; He, X.-X.; Liang, X.; Liu, S.-Z.; Lei, Z.-B.; Liu, Z.-H.; Peng, H.-L.; Zhang, J.; Kong, J.; Xu, H. Epitaxial growth of large-area and highly crystalline anisotropic $ReSe_2$ atomic layer. *Nano Res.* **2017**, *10*, 2732–274.
- (17) Dolui, K.; Rungger, I.; Das Pemmaraju, C.; Sanvito, S. Possible doping strategies for MoS_2 monolayers: An ab initio study. *Phys. Rev. B* **2013**, *88*, No. 075420.
- (18) Kochat, V.; Apte, A.; Hachtel, J.-A.; Kumazoe, H.; Krishnamoorthy, A.; Susarla, S.; Idrobo, J.-C.; Shimojo, F.; Vashishta, P.; Kalia, R.; Nakano, A.; Tiwary, C.-S.; Ajayan, P.-M. Re Doping in 2D Transition Metal Dichalcogenides as a New Route to Tailor Structural Phases and Induced Magnetism. *Adv. Mater.* **2017**, *29*, No. 1703754.
- (19) Lin, J.-H.; Zhou, J.-D.; Zuluaga, S.; Yu, P.; Gu, M.; Liu, Z.; Pantelides, S.-T.; Suenaga, K. Anisotropic Ordering in 1T Molybdenum and Tungsten Ditelluride Layers Alloyed with Sulfur and Selenium. *ACS Nano* **2018**, *12*, 894–901.
- (20) Lin, Y.-C.; Dumcenco, D.-O.; Komsa, H.-P.; Niimi, Y.; Krashennnikov, A.-V.; Huang, Y.-S.; Suenaga, K. Properties of Individual Dopant Atoms in Single-Layer MoS_2 : Atomic Structure, Migration, and Enhanced Reactivity. *Adv. Mater.* **2014**, *26*, 2857–2861.
- (21) Loh, L.-Y.; Chen, Y.-F.; Wang, J.-Y.; Yin, X.-M.; Tang, C.-S.; Zhang, Q.; Watanabe, K.; Taniguchi, T.; Wee, A.; Bosman, M.; Quek, S.-Y.; Eda, G. Impurity-Induced Emission in Re-Doped WS_2 Monolayers. *Nano Lett.* **2021**, *21*, 5293–5300.
- (22) Wang, Z.-X.; Zhao, X.-X.; Yang, Y.-K.; Qiao, L.; Lv, L.; Chen, Z.; Di, Z.-F.; Ren, W.; Pennycook, S.-J.; Zhou, J.-D.; Gao, Y.-F. Phase-Controlled Synthesis of Monolayer $W_{1-x}Re_xS_2$ Alloy with Improved Photoresponse Performance. *Small* **2020**, *16*, No. 2000852.
- (23) Miao, J.-L.; Zhang, F.-J. Recent Progress on Photomultiplication Type Organic Photodetectors. *Laser Photonics Rev.* **2019**, *13*, No. 1800204.
- (24) Gu, H.; Lu, Y.-M.; Zhu, D.-L.; Li, K.-L.; Zheng, S.-N.; Wang, J.-F.; Ang, K.-W.; Xu, K.; Liu, X.-K. High temperature study on the thermal properties of few-layer $Mo_0.5W_0.5S_2$ and effects of capping layers. *Results Phys.* **2017**, *7*, 4394–4397.
- (25) Qiao, H.; Yuan, J.; Xu, Z.-Q.; Chen, C.-Y.; Lin, S.-H.; Wang, Y.-S.; Song, J.-C.; Liu, Y.; Khan, Q.; Hoh, H.-Y.; Pan, C.-X.; Li, S.-J.; Bao, Q.-L. Broadband Photodetectors Based on Graphene- Bi_2Te_3 Heterostructure. *ACS Nano* **2015**, *9*, 1886–1894.
- (26) Cai, S.; Xu, X.-J.; Yang, W.; Chen, J.-X.; Fang, X.-S. Materials and Designs for Wearable Photodetectors. *Adv. Mater.* **2019**, *31*, No. 1808138.
- (27) Dalmatova, S.-A.; Fedorenko, A.-D.; Mazalov, L.-N.; Asanov, I.-P.; Ledneva, A.-Y.; Tarasenko, M. S.; Enyashin, A. N.; Zaikovskii, V. I.; Fedorov, V. E. XPS experimental and DFT investigations on solid solutions of $Mo_{1-x}Re_xS_2$ ($0 < x < 0.20$). *Nanoscale* **2018**, *10*, 10232–10240.
- (28) Yang, W.; Chen, J.-X.; Zhang, Y.; Zhang, Y.-J.; He, J.-H.; Fang, X.-S. Silicon-Compatible Photodetectors: Trends to Monolithically Integrate Photosensors with Chip Technology. *Adv. Funct. Mater.* **2019**, *29*, No. 1808182.
- (29) Yang, S.-Z.; Gong, Y.-J.; Manchanda, P.; Zhang, Y.-Y.; Ye, G.-L.; Chen, S.-M.; Song, L.; Pantelides, S.-T.; Ajayan, P.-M.; Chisholm, M.-F.; Zhou, W. Rhenium-Doped and Stabilized MoS_2 Atomic Layers with Basal-Plane Catalytic Activity. *Adv. Mater.* **2018**, *30*, No. 1803477.
- (30) Yang, D.-Z.; Ma, D.-G. Development of Organic Semiconductor Photodetectors: From Mechanism to Applications. *Adv. Opt. Mater.* **2019**, *7*, No. 1800522.
- (31) Wang, Y.; Song, L.; Chen, Y.; Huang, W. Emerging New-Generation Photodetectors Based on Low-Dimensional Halide Perovskites. *ACS Photonics* **2020**, *7*, 10–28.
- (32) Qiu, Q.-X.; Huang, Z.-M. Photodetectors of 2D Materials from Ultraviolet to Terahertz Waves. *Adv. Mater.* **2021**, *33*, No. 2008126.
- (33) Furchi, M.; Urich, A.; Pospischil, A.; Lilley, G.; Unterrainer, K.; Detz, H.; Klang, P.; Andrews, A.-M.; Schrenk, W.; Strasser, G.; Mueller, T. Microcavity-Integrated Graphene Photodetector. *Nano Lett.* **2012**, *12*, 2773–2777.
- (34) Gu, H.; Chen, L.; Lu, Y.-M.; Tian, F.-F.; Zhang, Z.-Q.; Xu, K.; Wu, J.; Botcha, V. D.; Li, K.-L.; Liu, X.-K. Low-temperature study of neutral and charged excitons in the large-area monolayer WS_2 . *Jpn. J. Appl. Phys.* **2018**, *57*, No. 060309.
- (35) Xie, Y.; Zhang, B.; Wang, S.-X.; Wang, D.; Wang, A.-Z.; Wang, Z.-Y.; Yu, H.-H.; Zhang, H.-J.; Chen, Y.-X.; Zhao, M.-W.; Huang, B.-B.; Mei, L.-M.; Wang, J.-Y. Ultrabroadband MoS_2 Photodetector with Spectral Response from 445 to 2717 nm. *Adv. Mater.* **2017**, *29*, No. 1605972.
- (36) Huang, Z.-Z.; Zhang, T.-F.; Liu, J.-K.; Zhang, L.-H.; Jin, Y.-H.; Wang, J.-P.; Jiang, K.-L.; Fan, S.-S.; Li, Q.-Q. Amorphous MoS_2 Photodetector with Ultra-Broadband Response. *ACS Appl. Electron. Mater.* **2019**, *1*, 1314–1321.
- (37) Xiao, Y.-F.; Min, L.; Liu, X.-K.; Liu, W.-J.; Younis, U.; Peng, T.-H.; Kang, X.-W.; Wu, X.-H.; Ding, S.-J.; Zhang, D.-W. Facile integration of MoS_2/SiC photodetector by direct chemical vapor deposition. *Nanophotonics* **2020**, *9*, 3035–3044.
- (38) Kang, P.-P.; Nan, H.-Y.; Zhang, X.-M.; Mo, H.-X.; Ni, Z.-H.; Gu, X.-F.; Ostrikov, K.; Xiao, S.-Q. Controllable Synthesis of Crystalline $ReS_{2(1-x)}Se_{2x}$ Monolayers on Amorphous SiO_2/Si Substrates with Fast Photoresponse. *Adv. Opt. Mater.* **2020**, *8*, No. 1901415.
- (39) Liu, X.-K.; Hu, S.-Q.; Luo, J.-L.; Li, X.-H.; Wu, J.; Chi, D.-Z.; Ang, K.-W.; Yu, W.-J.; Cai, Y.-Q. Suspended MoS_2 Photodetector Using Patterned Sapphire Substrate. *Small* **2021**, *17*, No. 2100246.
- (40) Liu, X.-K.; Hu, S.-Q.; Lin, Z.-C.; Li, X.-H.; Song, L.-J.; Yu, W.-J.; Wang, Q.; He, W. High-Performance MoS_2 Photodetectors Prepared Using a Patterned Gallium Nitride Substrate. *ACS Appl. Mater. Interface* **2021**, *13*, 15820–15826.
- (41) Cho, B.; Kim, A.-R.; Park, Y.; Yoon, J.; Lee, Y.-J.; Lee, S.; Yoo, T.-J.; Kang, C.-G.; Lee, B.-H.; Ko, H.-C.; Kim, D.-H.; Hahm, M.-G. Bifunctional Sensing Characteristics of Chemical Vapor Deposition Synthesized Atomic-Layered MoS_2 . *ACS Appl. Mater. Interface* **2015**, *7*, 2952–2959.
- (42) Zhang, J.-M.; Qian, Y.-Z.; Nan, H.-Y.; Gu, X.-F.; Xiao, S.-Q. Large-scale $MoS_{2(1-x)}Se_{2x}$ monolayers synthesized by confined-space CVD. *Nanotechnology* **2021**, *32*, 355601.